Check for updates

Huang Chen
Department of Mechanical Engineering,
Johns Hopkins University,
223 Latrobe Hall,
3400 N. Charles Street,
Baltimore, MD 21218
e-mail: hchen98@jhu.edu

Yuanchao Li
Department of Mechanical Engineering,
Johns Hopkins University,
223 Latrobe Hall,
3400 N. Charles Street,
Baltimore, MD 21218
e-mail: yli131@jhu.edu

David Tan
Department of Mechanical Engineering,
Johns Hopkins University,
223 Latrobe Hall,
3400 N. Charles Street,
Baltimore, MD 21218
e-mail: dtan4@jhu.edu

Joseph Katz[1]
Department of Mechanical Engineering,
Johns Hopkins University,
122 Latrobe Hall,
3400 N. Charles Street,
Baltimore, MD 21218
e-mail: katz@jhu.edu

Visualizations of Flow Structures in the Rotor Passage of an Axial Compressor at the Onset of Stall

Experiments preformed in the JHU refractive index matched facility examine flow phenomena developing in the rotor passage of an axial compressor at the onset of stall. High-speed imaging of cavitation performed at low pressures qualitatively visualizes vortical structures. Stereoscopic particle image velocimetry (SPIV) measurements provide detailed snapshots and ensemble statistics of the flow in a series of meridional planes. At prestall condition, the tip leakage vortex (TLV) breaks up into widely distributed intermittent vortical structures shortly after rollup. The most prominent instability involves periodic formation of large-scale backflow vortices (BFVs) that extend diagonally upstream, from the suction side (SS) of one blade at midchord to the pressure side (PS) near the leading edge of the next blade. The 3D vorticity distributions obtained from data recorded in closely spaced planes show that the BFVs originate form at the transition between the high circumferential velocity region below the TLV center and the main passage flow radially inward from it. When the BFVs penetrate to the next passage across the tip gap or by circumventing the leading edge, they trigger a similar phenomenon there, sustaining the process. Further reduction in flow rate into the stall range increases the number and size of the backflow vortices, and they regularly propagate upstream of the leading edge of the next blade, where they increase the incidence angle in the tip corner. As this process proliferates circumferentially, the BFVs rotate with the blades, indicating that there is very little through flow across the tip region.
[DOI: 10.1115/1.4035076]

Downloaded from http://asmedigitalcollection.asme.org/turbomachinery/article-pdf/139/4/041008/6305544/turbo_139_04_041008.pdf by Johns Hopkins University user on 08 December 2020

Introduction

When the flow rate is reduced, an axial compressor becomes less stable and more prone to stall or surge, phenomena that are detrimental to the performance of compressors [1–3]. Understanding how instabilities develop in the rotor passage and grow into a full scale stall, i.e., the stall inception, is important in developing tools to predict it and developing methods to mitigate its adverse effects [4]. In a developed state, multiple stall cells propagate circumferentially in a phase velocity that is typically lower than that of the rotor speed, a phenomenon typically referred to as rotating stall [5,6].

The precursors to stall are generally divided into two types, namely the long length-scale "modal-type" and the short length-scale "spike-type." Modal-type stall inception involves a long length-scale, wavelike circumferential velocity variations before stall cells appear [7–10]. In comparison, spike-type stall inception typically involves a large pressure spike at the endwall casing near the leading edge of the rotor [10–12] prior to stall. The exact reasons for spike-type stall are still debatable, in spite of the numerous experimental and computational studies attempting to elucidate it.

Surface-oil flow visualization and casing pressure measurement by Deppe et al. [11] show that spike formation involves leading-edge spillage and the trailing-edge backflow, proposed by Vo et al. [13] as the criteria for spike-type stall inception. Measurements by Inoue et al. [14,15] indicate that a large low-pressure region exists ahead of the rotor passage during stall, leading them to postulate the presence of a tornado-like vortex originating from leading edge separation, with one end at the suction side (SS) of the blade and the other at the casing. A similar interblade vortex has also been observed by Kosyna et al. within a single-stage axial-flow pump in deep stall [16]. Subsequent pressure measurement and simulation by Yamada et al. [17] agree with these findings and their relation to the onset of spike type stall. They show that the tornado-like separation vortex propagates circumferentially to the adjacent blade and induces separation there. Numerical simulations by Pullan et al. [18] indicate that the leading edge separation induced by high incidence at the rotor tip is the cause of spike-type stall. More importantly, they demonstrate that tip leakage flow is not a necessity in terms of leading edge separation or spike formation, although the leakage flow itself contributes to high incidence angle of the adjacent blade. Spike-type stall involving leading edge separation has also been observed computationally in centrifugal compressors [19].

A computational study by Hoying et al. [20] shows that the stall inception is caused by the interaction of the TLV with the leading edge of the adjacent blade when the TLV is aligned circumferentially at low flow rates. Simulations by Hah et al. [21] indicate that leading edge spillage and stall onset occurs when the tip leakage flow from one blade reaches the pressure side (PS) of the next blade.

Another type of large-scale instability occurring in the rotor passage has been called "rotating instability" by several researchers [4,22–25], although the specific nature of this phenomenon is still not resolved. März et al. [24] argued, based on an experimental and numerical study, that this phenomenon is caused by migration of low-pressure areas from one blade to the next. They show that the instabilities are more likely to happen for a large tip gap and attribute the low-pressure region to the leg of an axial vortex.

[1]Corresponding author.

Contributed by the International Gas Turbine Institute (IGTI) of ASME for publication in the Journal of Turbomachinery. Manuscript received September 20, 2016; final manuscript received September 28, 2016; published online January 10, 2017. Editor: Kenneth Hall.

 Copyright © 2017 by ASME

Many of the difficulties in identifying the mechanisms triggering stall inception are associated with difficulties in measuring 3D unsteady flow in the confined tip region of an axial turbomachine. To tackle this problem, the present study focuses on phenomena occurring prior to and at the onset of stall, based on flow visualizations and stereoscopic PIV (SPIV) measurements performed in the refractive index-matched facility at JHU. As previous tip leakage flow studies performed in this facility have shown [26–30], the unobstructed view enables us to identify the origin of flow structures and follow their development in the rotor passage. Results provide compelling evidence that the onset of stall involves development of backflow vortices originating from the interface between the backward tip leakage flow and the main passage flow near the SS of the rotor blade. They propagate diagonally upstream to the next passage either around the leading edge or across the tip gap of the adjacent blade. These structures appear to be similar to backflow vortex observed in more heavily loaded rocket inducers [31–33].

Experimental Setup

As described in Ref. [34], the blades of this one and a half stages axial turbomachine are based on the first one and a half stages of the low-speed axial compressor (LSAC) facility at NASA Glenn. However, while maintaining the same blade profiles, their aspect ratio has been modified to maintain a minimum thickness required for using acrylic blades in a liquid turbomachine. As shown in Fig. 1, the setup consists of a 20-blade inlet guide vane (IGV), a 15-blade rotor, and a 20-blade stator. The top nine IGV and stator blades and all 15 rotor blades are made of acrylic. The rest of the IGV blades are made of naval bronze, and they support the entire hub of the machine. The surfaces of the acrylic and the bronze blades are all polished, ensuring the roughness height in the submicron range. The casing is also made of acrylic with flat exterior surfaces to accommodate PIV measurements. Relevant dimensions are provided in Table 1. For the present measurements, the nominal tip gap is 1.8 mm, but due to manufacturing tolerances and slight eccentricities, the tip gap in the sample area is 2.4 mm.

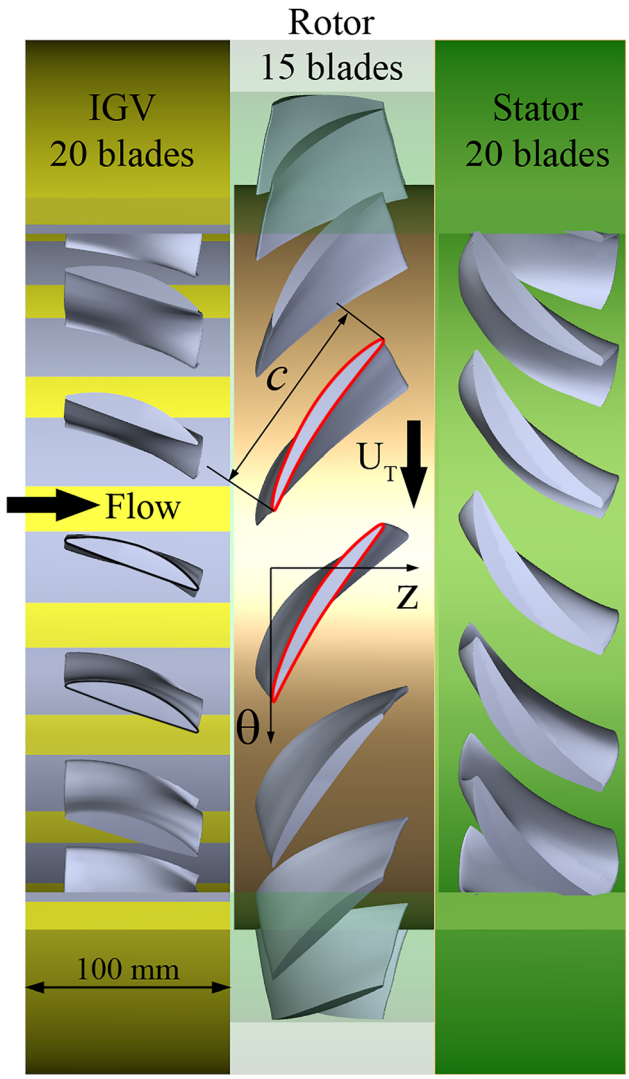

Fig. 1 Configuration of the one and a half stages compressor

The compressor is installed in the JHU closed loop optically index-matched facility whose description can be found in Refs. [26–28]. The working fluid is 62–63% by weight concentrated sodium iodide solution, whose refractive index, about 1.49, is matched with that of the acrylic blades and casing. The specific gravity of the solution is 1.8 and its kinematic viscosity at the experimental temperatures is about 1.1×10^{-6} m^2 s^{-1} [35]. Liquid temperature is maintained in the 20–25 °C range by a cooling system described in Ref. [28]. The machine is driven by a precision-controlled 44 kW AC motor via a 50.8 mm diameter shaft. The flow and pressure drop in the loop are controlled by an adjustable valve consisting of two perforated disks, which is installed in the return line. The mean pressure is controlled by connecting a half-filled tank located above the facility to a vacuum pump and a source of compressed nitrogen. Cavitation, which is used for visualizing vortical structures due to the low pressure in their cores, is induced by reducing the mean pressure in the facility. The visualization experiments have been performed numerous times at varying pressures, first to confirm that the occurrence and behavior of observed vortices are repeatable, and second, to verify that they are not affected, generated, or caused by the cavitation. The vortices appear consistently in all the experiments, and varying the pressure only changes the concentration of bubbles in the vortices but not their location and behavior. Furthermore, in Ref. [28], we compare the location of the TLV seen in the visualizations with that obtained in the PIV measurements. There is full agreement between them. All the SPIV measurements are performed at higher pressure, when cavitation is suppressed. More details about the present test facility are provided in Ref. [28].

All experiments are carried out at 480 RPM. The performance curves for the present tip gap are shown in Fig. 2. The static pressure rise across the pump is measured using pressure taps located upstream of the IGV and downstream of the stator. Each pressure tap is connected to two circumferentially distributed pressure ports to compensate for circumferential pressure variations in the inlet and outlet planes. The normalized static-to-static and total-to-static pressure coefficients are defined as

$$\psi_{SS} = (p_{exit} - p_{in})/(0.5\rho U_T^2) \quad (1)$$

Table 1 Stage relevant geometrical parameters

Casing diameter (D) (mm)	457.2
Hub diameter (d) (mm)	365.8
Rotor passage height (L) (mm)	45.7
Rotor diameter (D_R) (mm)	453.6
Rotor blade chord (c) (mm)	102.6
Rotor blade span (H) (mm)	43.9
Rotor blade stagger angle (γ) (deg)	58.6
Rotor blade axial chord (c_A) (mm)	53.5
Nominal tip clearance (mm)	1.8 (0.0175c or 0.041H)
Measured tip clearance (h) (mm)	2.4 (0.023c or 0.055H)
Shaft speed (Ω) (rad s^{-1}) {RPM}	50.27 {480}
Rotor blade tip speed (U_T) (m s^{-1})	11.47
Reynolds number ($U_T c/\nu$)	1.07×10^6

Downloaded from http://asmedigitalcollection.asme.org/turbomachinery/article-pdf/139/4/041008/6305544/turbo_139_04_041008.pdf by Johns Hopkins University user on 08 December 2020

$$\psi_{TS} = (p_{exit} - p_{0i})/(0.5\rho U_T^2) \quad (2)$$

The volumetric flow rate is measured by integrating the velocity profile obtained by translating a Pitot tube across the pipe in the return line. Thirteen equally spaced measurement points, starting from the centerline, with 12.7 mm intervals, are used for mapping the velocity distributions in the pipe. The flow rate coefficient is

$$\varphi = V_Z/U_T \quad (3)$$

where V_Z is the volumetric flow rate divided by the annular area of the rotor passage. Two differential pressure transducers are used to measure the static pressure rise from the pressure taps and the dynamic head from the Pitot tube. The signals are digitized at 3.3 kHz, and each performance point is based on averaging 200,000 data points. Each data point is recorded while operating the pump under the same condition for several minutes. The uncertainties associated with head rise and flow rate measurements are about 1.2% and 1.7%, respectively. Since the tip gap and flow rate have substantial impact on the performance of the machine and the flow structure within it, they are the primary focuses of a parallel paper, which includes results for $h/c = 0.5\%$ as well [36].

The present paper discusses SPIV measurements and cavitation visualizations performed at prestall conditions, namely at $\varphi = 0.25$. This point is chosen because it corresponds to the minimum possible stable operating flow rate. Further increase in pressure drop in the loop causes substantial fluctuations in performance. The performance curves shown in Fig. 2 includes all the data points obtained while operating the facility at fixed resistance and speed instead of continuously logging the pressure and flow rate as the compressor is throttled into stall, as suggested by Day [4]. As φ is reduced below 0.25, there is a certain narrow range ($0.24 < \varphi < 0.242$) for which we sometime observe further increase in pressure, and at other times, there is a sharp decrease in ψ accompanied by audible increase in noise and blade vibrations visible to a naked eye. We opt to include both data points. Once φ is reduced below 0.24, the noise and vibrations as well as the decrease in ψ_{SS} below 0.53 persist. Hence, we use $\varphi = 0.24$ as a representative for early stall conditions. Cavitation visualizations have been performed at both $\varphi = 0.25$ (and $\psi_{SS} = 0.56$) and $\varphi = 0.24$ (and $\psi_{SS} = 0.53$). As recommended by Day [4], Fig. 2(*b*) shows the performance in terms of total-to-static pressure coefficient as a better means of characterizing the performance slope near stall conditions. In this plot, the presently selected prestall condition resides slightly to the right of the peak ψ_{TS} point, namely when the performance curve still has a negative slope. As discussed later, this observation is included in the discussion about the type of stall occurring under this condition, following the criteria discussed in Ref. [10].

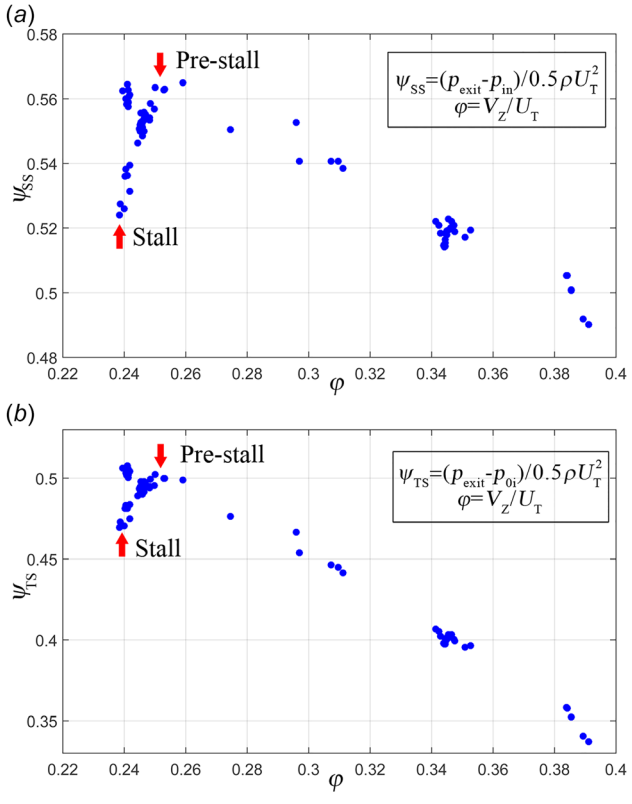

Fig. 2 (*a*) Static-to-static and (*b*) total-to-static performance curves at 480 RPM for an $h/c = 2.3\%$ tip gap

We have not performed SPIV measurements under stall conditions, in great part out of concern for the ability of the acrylic blades to withstand the unsteady loads and vibrations for prolonged periods. However, the flow visualizations described in this paper indicate that there is considerable similarity between flow instabilities under prestall and stall conditions. Hence, the measurements at $\varphi = 0.25$ provide ample data for characterizing flow instabilities involved with the onset of stall.

The experimental setup for SPIV measurements is shown in Fig. 3(*a*). The flow field is illuminated by a dual head, 200 mJ/pulse, Nd:YAG laser whose beam is expanded to a laser sheet with thickness of less than 1 mm, which illuminate meridional planes dissecting the rotor blade at different chord fractions. The pulse delay between pulses is 20 μs. The flow is seeded with 13 μm, silver-coated hollow spherical glass particles that have a specific gravity of 1.6, slightly lower than that of the fluid. A pair of PCO© 2000, interline transfer cameras with resolutions of 2048×2048 pixels are mounted on different sides of the laser sheet. Each camera is equipped with a 105 mm macrolens mounted on a Scheimpflug adaptor to satisfy the imaging conditions. To reduce image distortion and multiple reflections, the sample area is viewed through an acrylic prism whose external surfaces are perpendicular to the optical axes of the lenses. Both cameras are mounted as a unit on a precision-controlled vertical motorized slide. Calibration is carried out following the two-step procedure described by Wieneke [37]. First, coarse calibration is performed based on images of a target immersed in a calibration chamber and filled with the same fluid, which is located above the compressor. Then, fine calibration is performed based on a series of particle images recorded within the sample volume. As illustrated in Fig. 4, SPIV measurements have been conducted over a series of meridional planes.

During analysis, the SPIV images are preprocessed, first by filtering out the background noise and image nonuniformities [38], and then enhanced by applying a modified histogram equalization algorithm [39]. Multipass FFT-based cross-correlations of image pairs are carried out using the LaVison© DaVis commercial software package. The final interrogation window size is 32×32 pixels with 50% overlap, corresponding to a vector spacing of 0.16 mm (field of view 20.41×29.13 mm^2) in measurement planes upstream of $s/c = 0.16$, and 0.17 mm (field of view 23.1×31.7 mm^2) for the rest of the planes afterward. Universal outlier detector filters described by Westerweel and Scarano [40] are adopted to reject bad vectors during vector postprocessing. The uncertainty in instantaneous velocity is in the order of ~0.1 pixel as long as there are more than five particles within each interrogation window [27]. The present results are presented in a cylindrical coordinate system with the origin located at the center of the machine, and the axial and circumferential directions coinciding with the rotor blade leading edge (Figs. 1 and 4). The location of sample planes is defined as s/c, where s is chordwise distance from the leading edge. The corresponding velocity components are u_z, u_r, u_θ. Ensemble-averaged statistics presented in this paper, which as denoted by $< >$, is based on averaging 2500

Downloaded from http://asmedigitalcollection.asme.org/turbomachinery/article-pdf/139/4/041008/6305544/turbo_139_04_041008.pdf by Johns Hopkins University user on 08 December 2020

instantaneous realizations obtained for the same condition and chordwise location. Velocity fluctuations are defined as $u_i' = u_i - \langle u_i \rangle$.

The experimental setup for cavitation visualization is shown in Fig. 3(*b*). Two continuous halogen lamps are placed at both sides of the pump and illuminate the tip region of the rotor passage. The PCO© dimax high-speed camera has a CMOS sensor of 2016×2016 pixels, but 1536×1332 pixels images are recorded to accommodate an acquisition rate of 2400 frames/s, corresponding to 20 images per blade passage period. The field of view is 140.6×163.4 mm^2.

Results and Discussion

Mean Flow Characteristics. Sample ensemble-averaged circumferential vorticity ($\langle \omega_\theta \rangle$) and velocity ($\langle u_\theta \rangle$) obtained at prestall conditions, $\varphi = 0.25$, are shown in Fig. 5. Circumferential vorticity in the cylindrical coordinate system is defined as

$$\omega_\theta = \frac{\partial u_r}{\partial z} - \frac{\partial u_z}{\partial r} \tag{4}$$

Here, $\langle u_\theta \rangle$ is normalized by the tip speed and $\langle \omega_\theta \rangle$ by the rotational speed of the machine (in rad/s). They are chosen to follow the TLV development, from the vicinity of the leading edge, midchord, and aft parts of the rotor passage as a baseline for subsequent discussions. At $s/c = 0.16$, the TLV is in its early stage of development, but there is already a strong backward leakage flow across the tip gap, from the PS to the SS of the blade. It meets the main passage flow at $z/c = -0.03$, located upstream of the plane of the blade leading edge, creating a local stagnation point there (not shown). The average vorticity peaks around the TLV center and around the PS tip corner. However, it should be noted that in instantaneous "snapshots" of the flow, the vicinity of the TLV center contains multiple interlacing vortex filaments that never merge into a distinct vortex, as demonstrated by the sample in Fig. 6 and in previous studies involving several turbomachines and operating conditions [26–30]. Figure 6 also serves as a baseline image of the flow around an unstalled blade tip. At $s/c = 0.33$, the TLV grows in size and detaches from the blade but remains connected to SS tip by a shear layer that keeps on feeding vorticity into it. At $s/c = 0.76$, the average peak vorticity magnitude within the TLV is substantially lower than that in previous planes, but it is spread over a large area. As discussed in Ref. [28] for the same condition, as well as reported in previous studies [26–30,41–43], this rapid expansion is caused by bursting/breakup of the TLV. When it occurs, presumably because of adverse pressure gradients in the aft parts of the passage and migration to the PS of the next

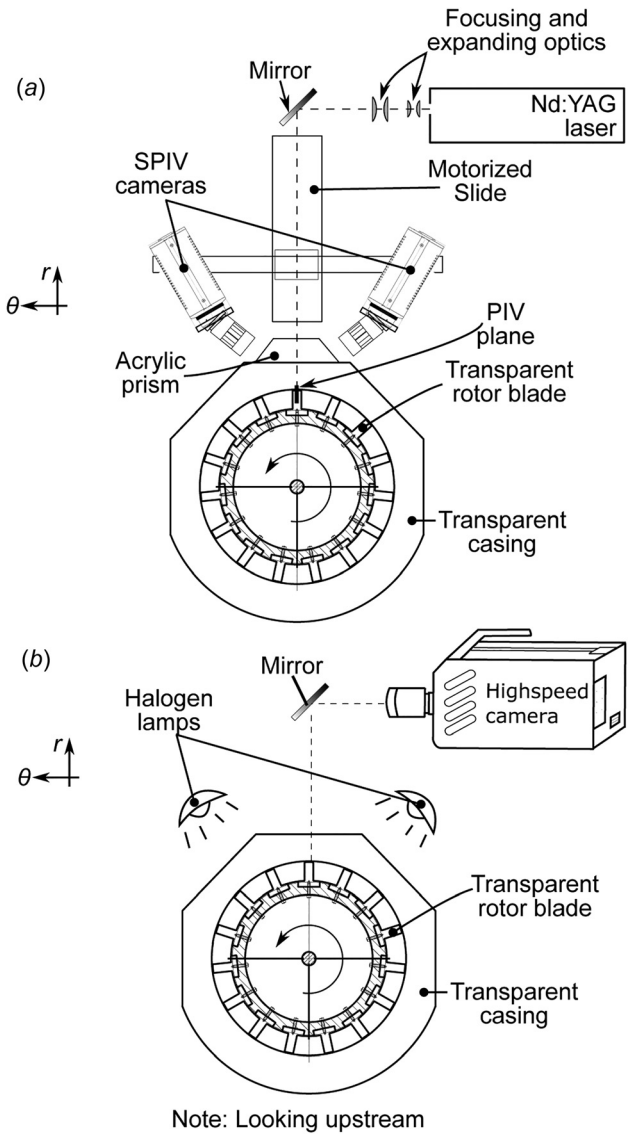

Fig. 3 Setups for (*a*) SPIV in meridional planes and (*b*) cavitation flow visualization

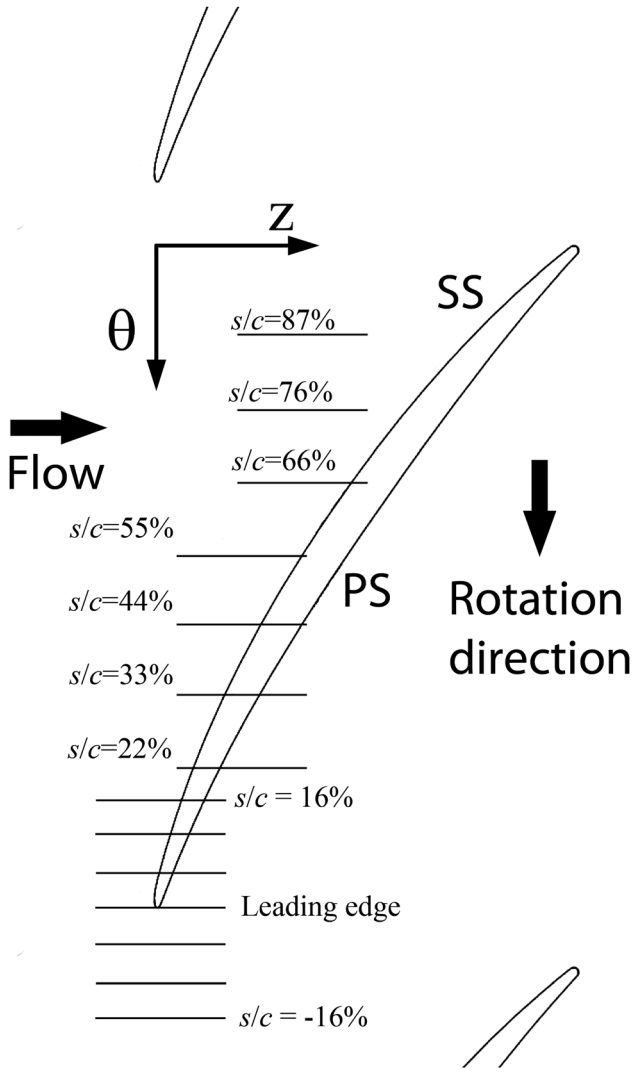

Fig. 4 Rotor blade tip profile with horizontal lines highlighting the SPIV measurement sample areas

Downloaded from http://asmedigitalcollection.asme.org/turbomachinery/article-pdf/139/4/041008/6305544/turbo_139_04_041008.pdf by Johns Hopkins University user on 08 December 2020

blade, the vortex filaments become randomly scattered over an area that cover a substantial fraction of the passage.

Two distinct areas with elevated $<u_\theta>$ are evident in the distribution presented in Figs. 5(*b*), 5(*d*), and 5(*f*). The first broad area is located in the PS of the blade, and the second is centered radially inward (under) and slightly upstream of the TLV. These high $<u_\theta>$ regions actually contain fluid moving in the same circumferential direction as the blade. Combined with the low values of $<u_z>$ there, especially to the left of and immediately under the TLV, the velocity distributions indicate that substantial fractions of the tip region are blocked. The size and the magnitude $<u_\theta>$ under the TLV grow substantially with increasing chord fraction (and with decreasing flow rate—see Ref. [36]), especially after vortex breakup. In fact, the high circumferential velocity on the PS in Figs. 5(*b*) and 5(*d*) is associated with migration of the TLV generated by the previous/adjacent blade to the pressure side of this blade. This phenomenon has also been reported by previous experimental studies [26,44,45]. It is caused by entrainment of fluid originating from the tip gap, which attains the blade circumferential momentum. It is also affected by exposure to adverse pressure gradients during its propagation in the passage to the PS of the next blade. As will be shown later, formation of high $<u_\theta>$ zones in the tip region plays a role in processes affecting the onset of stall.

Sample distributions of turbulent kinetic energy (TKE), defined as

$$k^* = 0.5(\overline{u_z'u_z'} + \overline{u_r'u_r'} + \overline{u_\theta'u_\theta'})U_T^{-2} \tag{5}$$

are shown in Fig. 7. They are presented to highlight the regions of high flow instabilities, especially under prestall conditions. To demonstrate the associated enormous increase in turbulence, Fig. 7(*d*) shows the distribution of TKE $s/c = 0.33$ for $\varphi = 0.35$, at the same location as Fig. 7(*b*), for which results have to be presented at a significantly different scale to be visible. For all the cases corresponding to $\varphi = 0.25$, the TKE is high around the TLV center, to a substantial part due to fluctuations in the distributions of vortex filaments around the mean core. Once bursting occurs (Fig. 7(*c*)), the high TKE area grows substantially, occupying a large fraction of the rotor passage, all the way to the PS of the adjacent blade (Figs. 7(*a*) and 7(*b*)). Other large-scale flow instabilities, which affect the onset of stall, are also involved, as described in the next section, Visualization of Flow Structures at Pre-Stall Conditions. At $s/c = 0.33$ (and to a lesser extent also at $s/c = 0.16$), the TLV turbulence on the PS is ingested to the SS of the blade through the tip gap, affecting the flow stability there. This plot provides statistical evidence demonstrating the crosstalk among passages, which is facilitated by tip leakage flow across the relatively wide clearance of the present configuration. Such interactions are minimal for narrow gaps, e.g., for $h/c = 0.5\%$ [36]. This crosstalk contributes to the development of instabilities on the SS side of the machine prior to stall. The resulting substantial decrease in flow stability is demonstrated by the comparison between Figs. 7(*b*) and 7(*d*). At $\varphi = 0.35$, secondary structures associated with the previous TLV arrive to the next blade much further downstream in the rotor passage and have much less impact on the flow stability.

Visualization of Flow Structures at Prestall Conditions. A time sequence of high-speed images demonstrating the evolution of vortical structures in the rotor passage is presented in Fig. 8. Here, the time is normalized by blade passage period

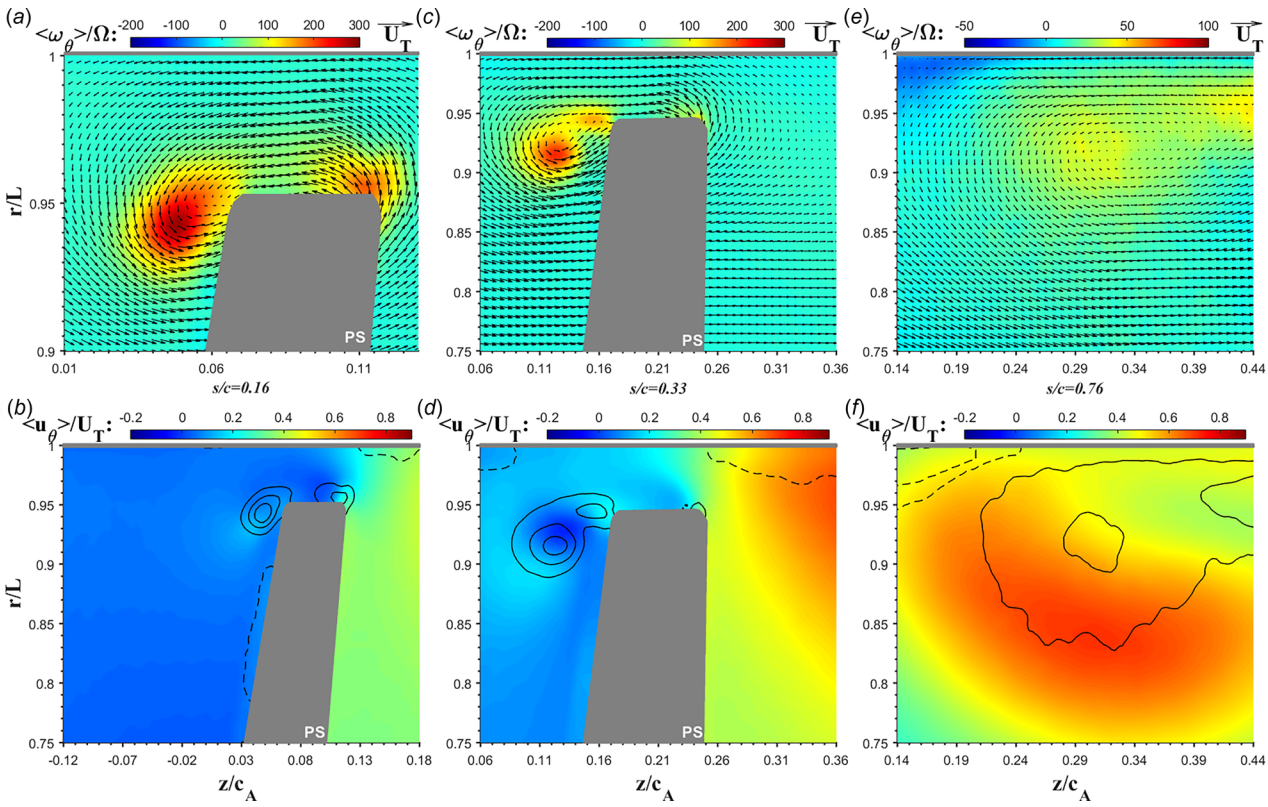

Fig. 5 Ensemble-averaged contours of $<\omega_\theta>$ (top row) and $<u_\theta>$ (bottom row) at: (*a*) and (*b*) $s/c = 0.16$, (*c*) and (*d*) $s/c = 0.33$, and (*e*) and (*f*) $s/c = 0.76$. Lines in (*b*), (*d*), and (*f*) are contours of $<\omega_\theta>$, with dashed lines indicating negative values. Vectors in (*a*) are shown in full resolution for part of the sample area. In (*c*) and (*e*), vectors are diluted by 2:1 axially and 2:1 radially for clarity. Note the differences in vorticity scale. A reference vector showing the tip speed is provided on top. Horizontal axis is the streamwise direction while vertical axis is the radial direction. Other plots of SPIV results follow the same convention.

Downloaded from http://asmedigitalcollection.asme.org/turbomachinery/article-pdf/139/4/041008/6305544/turbo_139_04_041008.pdf by Johns Hopkins University user on 08 December 2020

$$t^* = (t - t_0)/(2\pi/15\Omega) \quad (6)$$

The TLV rolls up very near the tip of the leading edge but quickly breaks down into a series of secondary structures (Fig. 8(*a*)). More interestingly, apart from the TLV, another vortical structure aligned perpendicularly to the blade develops and propagates from the leading edge to midchord. Arrows of the same style highlight its location in different fames.

At $t^* = 0$, it starts as a small filament under the TLV near the blade leading edge. As it migrates downstream, this structure increases in length, with one end just about following the tail of the TLV, and the other extending diagonally upstream, while getting closer in time to the leading edge of the next blade. The rotation direction of this vortex, determined by following vortical structures in time in the high-speed movies of cavitation, is that the vorticity points at the SS of the originating blade. This direction is also consistent with the SPIV data discussed later. Because of its orientation, and terminology used in prior studies detecting similar structures in other turbomachines (Refs. [31–33], details follow), we refer to this structure as a backflow vortex or BFV. As

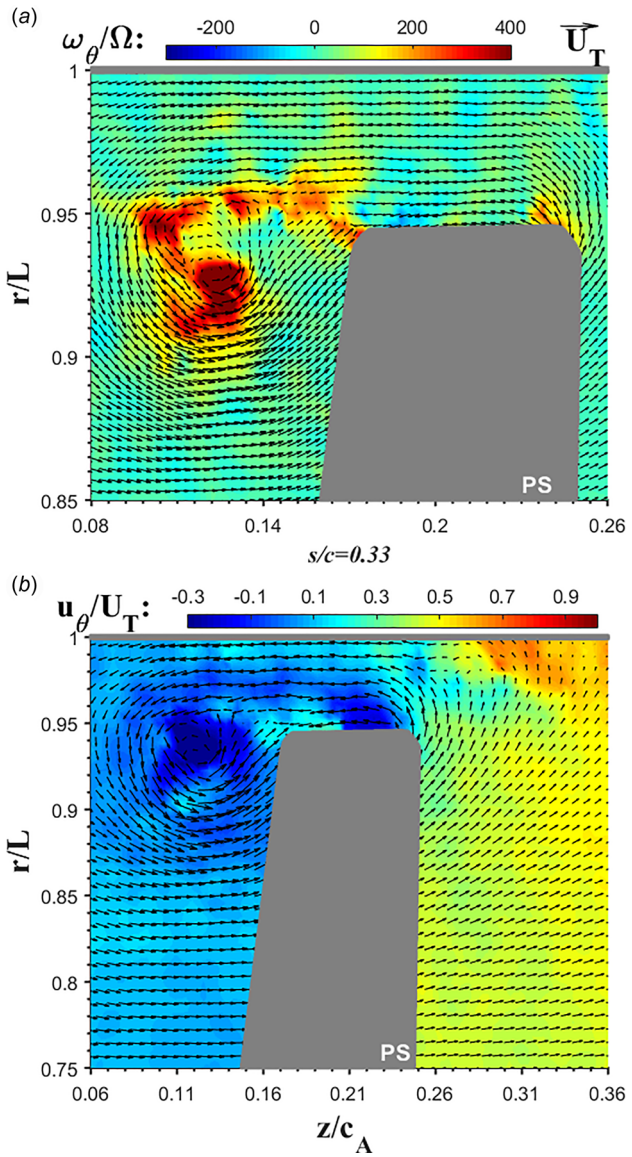

Fig. 6 A sample instantaneous realization of (*a*) ω_θ and (*b*) u_θ at $s/c = 0.33$, representing conditions when the blade tip is not stalled. Vectors in (*b*) are diluted by 2:1 axially and 2:1 radially. Note the differences in scales.

it grows, the orientation of the BFV diagonally upstream does not change significantly. Since this vortex is largely transported with the blade circumferentially, and its outward end remains at nearly the same axial plane ($z \sim 0$), it implies that there is very little through flow in the tip region. At $t^* = 0.45$ (Fig. 8(*d*)), the vortex seems to be strong enough to alter the trajectory of the end of the TLV. At $t^* = 0.75$, the upstream end of the vortex reaches the leading edge of the next blade, and at $t^* = 0.9$, its end penetrates the tip gap. Additional evidence recorded at a different time that the vortex extends across the tip gap is provided in Fig. 9(*b*) at a higher magnification. At $t^* = 1.05$ (Fig. 8(*h*)), the backflow vortex (or structures associated with it) appears to be split by the blade into two sections, leaving a short segment, which is marked by another arrow, on the suction side. Subsequently, as Figs. 8(*i*) and 8(*j*) show, this segment grows and forms a structure that appears to be quite similar to that shown in Fig. 8(*a*). Indeed, at later times (not shown), this vortex continues to grow and propagates to the next blade, following a sequence that is very similar to that presented in Figs. 8(*a*)–8(*i*). Based on examination of the movies (including the sample shown), the phase speed of what appears to be a circumferentially propagating periodic pattern is slower than the blade rotational speed by about 30–40%. By comparing the locations of initial TLV rollup in Figs. 9(*a*) and 9(*b*), it is evident that rollup of the TLV is delayed when the upstream end of the backflow vortex arrives at the leading edge of the next blade or crosses the tip gap. Such a change indicates a considerable shift in the distribution of blade loading. In addition, when SS end of this vortex reaches trailing part of the TLV, it appears to be sufficiently powerful to disrupt the development of TLV (Figs. 8(*d*) and 8(*e*)). Hence, development and propagation of the vortex causes subsynchronous rotating disruption to both the blade performance and the entire flow in the rotor passage. Both are phenomena associated either with the inception of rotating stall or rotating instabilities discussed in Refs. [4] and [22–25].

The observations described above raise a question of where does the BFV come from, and what is the origin of its vorticity. Since during early phases of development, the vortex appears to protrude diagonally upstream from under the TLV, and recalling that there is a region of elevated $<u_\theta>$ below TLV, one questions whether they are related. Selecting $s/c = 44\%$ for further discussion, this relationship is elucidated by examining the 3D ensemble-averaged velocity and vorticity distributions in the tip region. First, the distributions of $<u_\theta>$, $<u_z>$, and $<u_r>$ are shown in Figs. 10(*a*)–10(*c*), and the velocity diagram is shown in Fig. 10(*d*). Two points are selected as representatives, the first from the high $<u_\theta>$ region under the TLV (A) and the second from the low $<u_\theta>$, but high $<u_z>$ region below the area influenced by the tip leakage (B). Corresponding values of $<u_\theta>$ and $<u_z>$ are tabulated and illustrated in Fig. 10(*d*), along with the projection of the relative velocity between B and A in the z–θ plane, The relative velocity $<u_{\text{B-A}}>$, which is indicated by the red arrow, is nearly parallel to the blade chord. Hence, if the shear layer under the high $<u_\theta>$ region rolls up into a vortex due to some perturbation, the primary vorticity direction would be nearly perpendicular to the blade chord, as indicated by the direction of ω_{BFV}. This conceptual, but data-based, discussion is consistent with the direction and orientation of the BFVs in Figs. 8 and 9. The large upstream propagating vortex might originate from rollup of the shear layer located at the interface between the high $<u_\theta>$ region (TLV induced blockage) and the through flow under it.

Further evidence is provided by the sample average three-dimensional vorticity distributions in Figs. 10(*e*)–10(*h*). To determine the ensemble-averaged derivatives of velocity in the circumferential direction ($\partial/\partial\theta$) required for calculating the 3D vorticity components, we have recorded data in 11 closely spaced meridional planes, which are separated by an angular distance of 3.6×10^{-4} rad. The corresponding circumferential distance between planes is 0.081 mm at the casing and 0.073 mm at the bottom of the field of view, namely it is smaller than the in-plane

Downloaded from http://asmedigitalcollection.asme.org/turbomachinery/article-pdf/139/4/041008/6305544/turbo_139_04_041008.pdf by Johns Hopkins University user on 08 December 2020

vector spacing. In each plane, 2500 realizations are ensemble-averaged to obtain the distributions of all three velocity components, like the rest of the data. Using second-order finite differencing, the vorticity components involving out-of-plane derivatives are obtained from

$$\omega_z = \frac{1}{r}\frac{\partial}{\partial r}(ru_\theta) - \frac{1}{r}\frac{\partial u_r}{\partial \theta} \tag{7}$$

$$\omega_r = \frac{1}{r}\frac{\partial u_z}{\partial \theta} - \frac{\partial u_\theta}{\partial z} \tag{8}$$

To improve the data quality, we use the data from all the 11 planes, by circumferentially averaging vorticity distributions calculated from planes 1 and 3, planes 2 and 4, planes 3 and 5, and so on. Figures 10(*e*)–10(*g*) show the resulting distributions of all three vorticity components at $s/c = 0.44$, where $<\omega_\theta>$, the largest component, is based on the in-plane data. Compared with $<\omega_\theta>$ at $s/c = 0.33$ shown in Fig. 5(*c*), the TLV is clearly larger, but the peak vorticity decreases, indicating the TLV has already started to burst. However, most important for the present discussion is the broad area of elevated $<\omega_z>$ centered around point (C) in Fig. 10(*f*). This region is located in the region of radial gradients in $<u_\theta>$ under the TLV, at the transition between the high $<u_\theta>$ zone surrounding the TLV and the main passage flow. The values of $<\omega_\theta>$ and $<\omega_z>$ in point (C) are tabulated in Fig. 10(*h*), along with a plot of the resulting projection of the vorticity in the z–θ plane. The orientation of the vorticity projection in the z–θ plane is consistent with the orientation of the backflow vortex seen in the cavitation images in Figs. 8 and 9, and the velocity vectors in Fig. 10(*d*). The mean vorticity distributions indicate that the underlying flow phenomenon causing the formation of the BFV is the radial gradients in $<u_\theta>$ under the TLV, which persists along the entire blade. While mean vorticity in this region is substantially lower than $<\omega_\theta>$ near the TLV center, once the BFV rolls up intermittently and stretched by the strain field in the passage, the cavitation images suggest that its core vorticity becomes large (further discussion follows).

Figures 10(*f*) and 10(*g*) also show that the TLV center is located in a region of negative $<\omega_z>$, and the distribution of $<\omega_r>$ is also nonuniform, with both positive and negative regions. To explain the 3D flow structure that these patterns represent, Fig. 10(*i*) provides a 3D depiction of the distribution of circumferential velocity, where the out of the plane protrusion is proportional to $<u_\theta>$, and Fig. 10(*j*) sketched the origin of vortical layers emerging from the tip gap superimposed on the distribution of $<u_\theta>$. The magnitudes and directions of $<\omega_z>$ and $<\omega_r>$ coincide with radial and axial gradients in $<u_\theta>$, respectively. These vortical regions are originated from the tip gap and could be elucidates as a combined effect of three layers (Fig. 10(*j*)) with different vorticity distributions. The inner layer starts at the SS tip corner and carries substantial circumferential vorticity directly into the TLV center. The associated $<\omega_z>$ is positive, consistent with the positive radial gradients in $<u_\theta>$ at the interface between

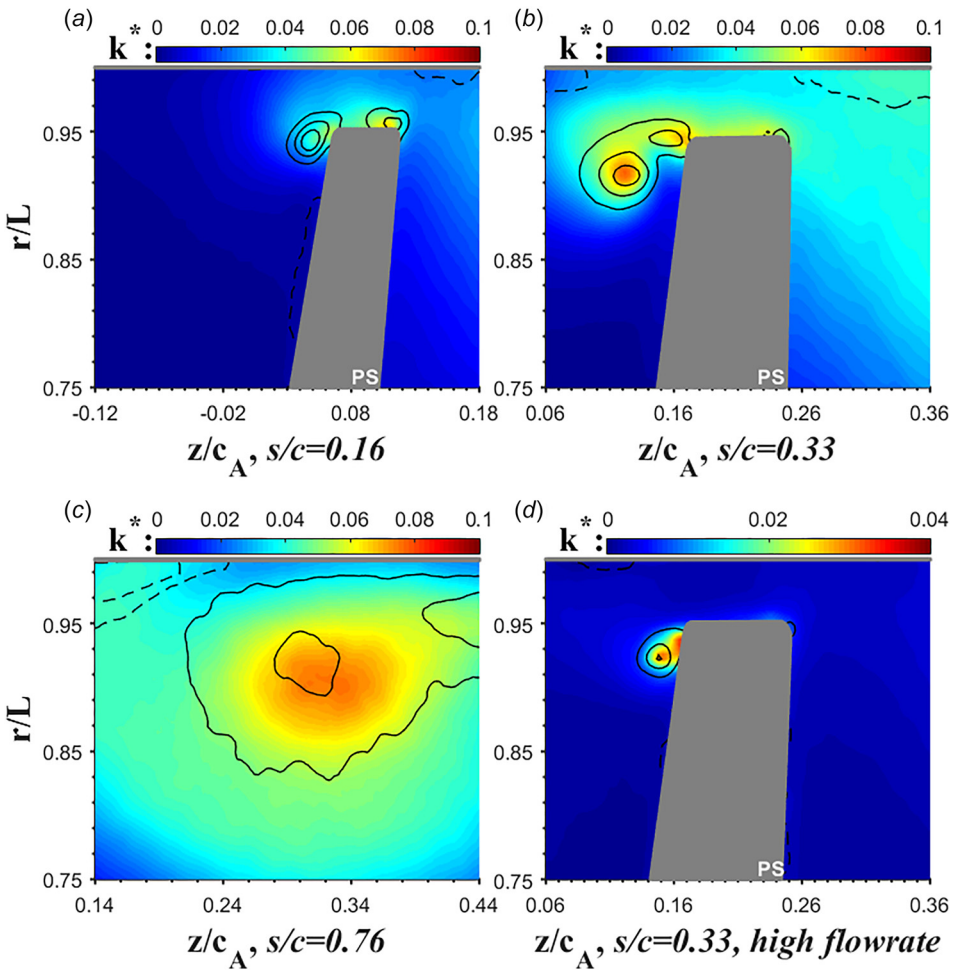

Fig. 7 Contours of the TKE at (*a*) $s/c = 0.16$, (*b*) $s/c = 0.33$, and (*c*) $s/c = 0.76$ at $\varphi = 0.25$. (*d*) TKE at $\varphi = 0.35$ and $s/c = 0.33$, the same location as (*b*), aimed at highlighting differences between them. Note the differences in scale. Lines are contour of $<\omega_\theta>$, with dashed lines indicating negative values.

Downloaded from http://asmedigitalcollection.asme.org/turbomachinery/article-pdf/139/4/041008/6305544/turbo_139_04_041008.pdf by Johns Hopkins University user on 08 December 2020

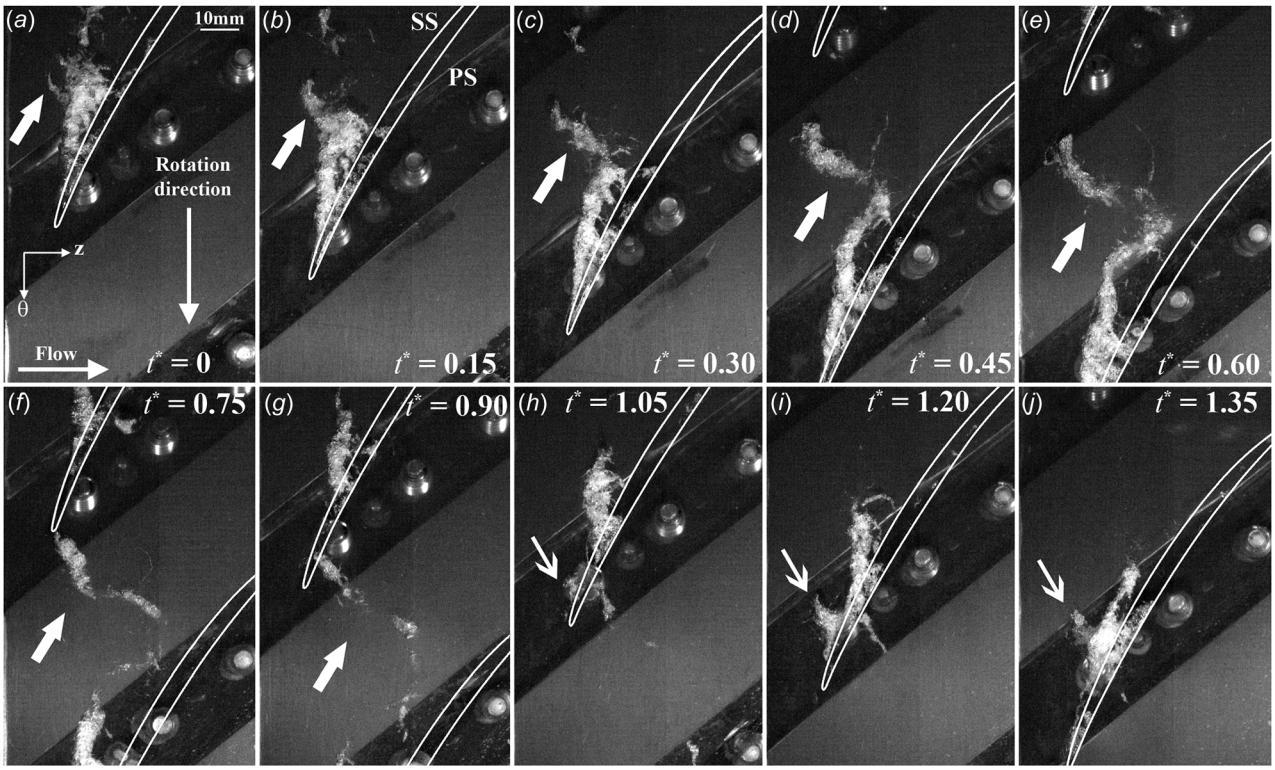

Fig. 8 A time sequence of cavitation images showing the propagation of vortical structures at prestall conditions. Arrows of same styles follow the evolution of the same backflow vortex. White lines indicate the blade tip profile.

the leakage flow and the passage flow under. As this layer is entrained by the TLV, the positive $<\omega_z>$ becomes positive $<\omega_r>$, then negative $<\omega_z>$. The second layer follows the other side of the elevated $<u_\theta>$ region, as it emerges from the tip gap. It starts as a negative $<\omega_z>$ in the tip gap, consistent with the radial decrease in $<u_\theta>$ between the blade and the endwall casing. As this layer circumvents the TLV, the negative $<\omega_z>$ becomes negative $<\omega_r>$ to the left of the TLV, positive $<\omega_z>$ under the TLV, and finally positive $<\omega_r>$ to the right of the TLV. The flow field has a third outer layer, which contains fluid originating from the endwall boundary layer. This layers separates from the endwall when the leakage flow meets (impinges on) the main passage flow. Only parts of this layer are shown on the right sides of the distributions presented in this paper [26,28,36]; hence, it is sketched using a dashed line in Fig. 10(*j*). This discussion suggests

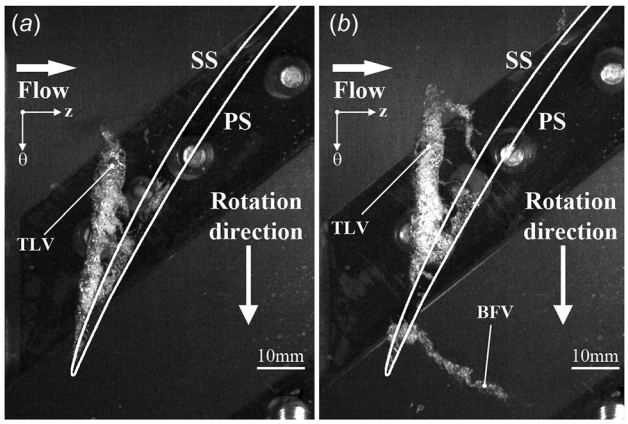

Fig. 9 Sample cavitation images showing (*a*) TLV without the influence of the backflow vortex and (*b*) the backflow vortex propagating across the tip gap

that the backflow vortices evident in the cavitation images originate from the outer layer of a "ringlike" vortical structure that surrounds the TLV. As discussed later, we have seen very similar mutlilayer phenomena in other axial waterjet pumps [26]. Hence, the flow structure illustrated in Fig. 10(*j*) is not unique to the present compressor. Furthermore, the present depiction bears several similarities to the partial vortical ring surrounding the TLV and leading edge separation in Refs. [17] and [18], except that in their depiction, the layers connects to the endwall and to the blade surface.

The present observations and conjectures are consistent with several prior studies. First, they agree with experimental and numerical studies focusing on the development of so-called backflow vortices in rocket inducers by Yamanishi et al. [31] and Yokota et al. [46]. They show that in heavily loaded inducers, where the strong leakage flow extends upstream of the rotor ("backflow"), the backflow vortices are caused by interaction of the swirling backflow and the forward flow under it. Although there are some differences in magnitudes, orientations and specific flow structures involved, the origin of the present observed propagating/rotating instability is still interaction of the main passage flow with the region dominated by the leakage flow. Hence, we opt to also refer to the present phenomenon as "backflow vortex (BFV)," following Refs. [31–33] and [46]. Next, in previous measurements within a waterjet pump performed within this index-matched facility, SPIV data obtained in a series of closely spaced parallel meridional planes have also enabled calculation of the ensemble-averaged 3D vorticity distribution [26]. Results show a region of concentrated streamwise vorticity radially inward from the high $<u_\theta>$ region under the TLV. The associated vorticity magnitude, about 50% of the circumferential vorticity in the TLV core, is substantial, confirming the presence of a powerful shear layer there.

Since the present SPIV measurements only allow us to calculate the ensemble-averaged $<\omega_r>$ and $<\omega_z>$, and as the cavitation images show, formation of the backflow vortex is intermittent, it is difficult to discern its presence from the vorticity distributions

Downloaded from http://asmedigitalcollection.asme.org/turbomachinery/article-pdf/139/4/041008/6305544/turbo_139_04_041008.pdf by Johns Hopkins University user on 08 December 2020

in the relevant region (Figs. 5 and 10). However, since the present backflow vortex is aligned diagonally, snapshots of its signature and impact on the flow around the leading edge and tip gap should be readily seen in the part of the 2500 instantaneous realizations for each plane. Indeed they are! Selected instantaneous realizations of ω_θ and u_θ for the same s/c as Fig. 5 are presented in Fig. 11. In all three examples, regions of high u_θ that increase in size with s/c, wrap around the mean TLV center. At $s/c = 0.76$, the layer appears to be connected to the endwall casing, but in plots showing the blade, the high u_θ zone originates from the tip gap. Outside of this region u_θ is small, indicating large radial and axial gradients in u_θ (depending on the orientation of the interface) at the interface between these area regions. It is possible that these gradients involve high axial and radial vorticity, respectively, as well. Furthermore, a series of distributed circumferential vortex fragments/filaments with high vorticity appear to be distributed along the boundary of the high u_θ region indicated by the arrows, clearly well below the TLV center. Combined with the analyses of ensemble-averaged results shown in Fig. 10, this picture strongly indicates that the backflow vortex exists at the border of the high u_θ region and the main passage flow and circles around the TLV. The instantaneous snapshots show that the underside of the high u_θ region contains multiple filaments distributed along the boundary of a flow domain jetting in the circumferential direction, essentially at the blade speed.

Moreover, Figs. 11(*c*) and 11(*d*) show a series of elevated ω_θ regions coinciding with the underside of the high u_θ zone on the PS of the blade being entrained into the tip gap. As these BFVs crossed the gap, they interact with the TLV on the SS, causing the latter to deviate from its "normal" shape shown in Fig. 6. In addition, the flow structure shows early signs that new BFVs begin to rollup into distinct vortices well below the TLV, at $r/L \sim 0.85$,

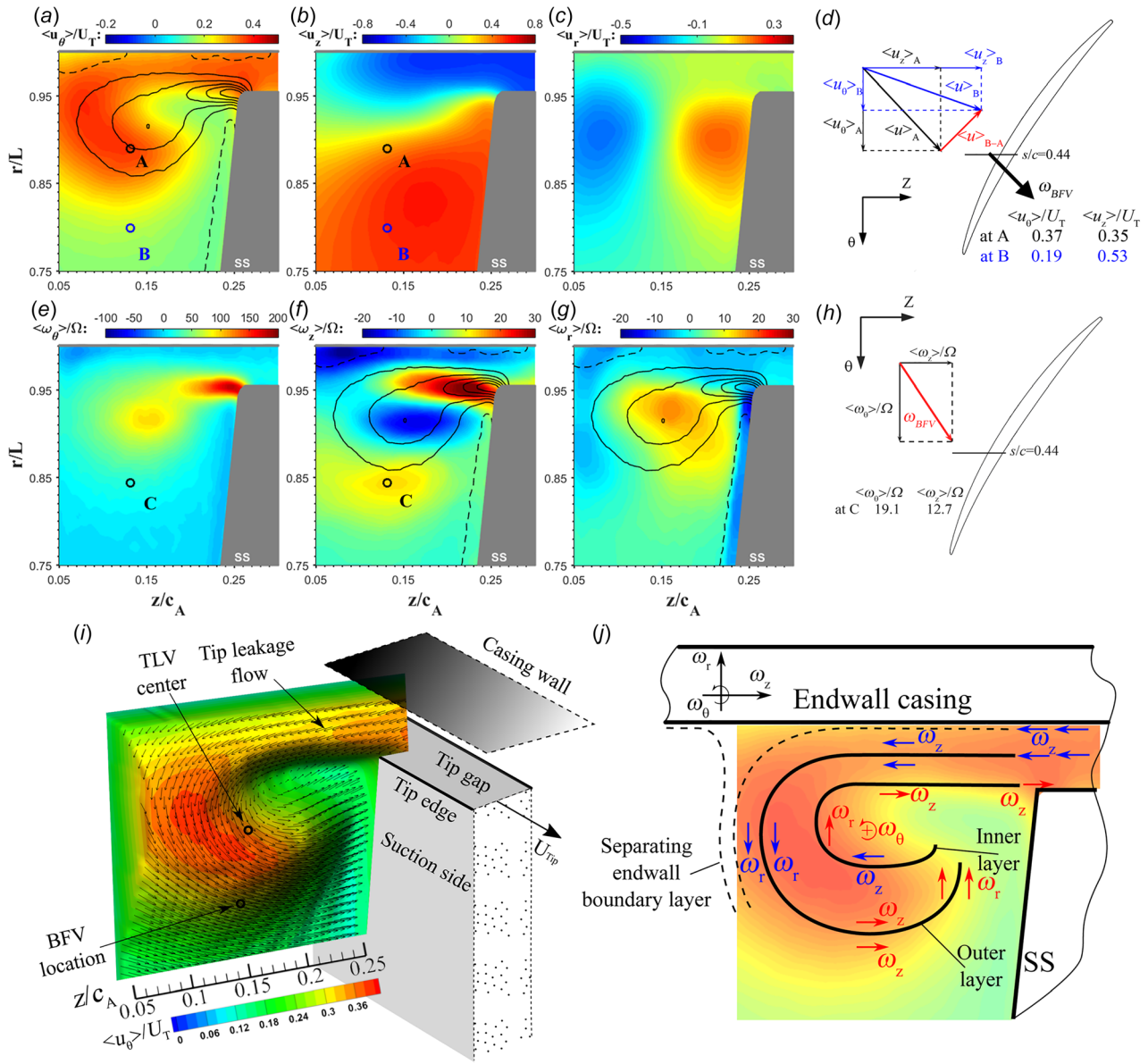

Fig. 10 Ensemble-averaged three-dimensional velocity and vorticity distributions in the meridional plane at $s/c = 0.44$ and $\varphi = 0.25$. (*a*)–(*c*) Plots of $\langle u_\theta \rangle$, $\langle u_z \rangle$, and $\langle u_r \rangle$. (*d*) Velocity diagram for points A and B, explaining the orientation of the backflow vortices. (*e*)–(*g*) Distributions of $\langle \omega_\theta \rangle$, $\langle \omega_z \rangle$, and $\langle \omega_r \rangle$. (*h*) Vorticity diagram for point C, explaining the direction of the backflow vortices. (*i*) Perspective view of circumferential velocity distribution with three-dimensional velocity vectors. The elevation of the protruding surface is proportional to $\langle u_\theta \rangle$. Vectors are diluted by 2:1 axially and radially. (*j*) Sketch of vortical layers originating from the tip gap, and surrounding the TLV. Background is the $\langle u_\theta \rangle$ contour. Lines in (*a*), (*f*), and (*g*) are contours of $\langle \omega_\theta \rangle$, with dashed lines indicating negative values.

Downloaded from http://asmedigitalcollection.asme.org/turbomachinery/article-pdf/139/4/041008/6305544/turbo_139_04_041008.pdf by Johns Hopkins University user on 08 December 2020

coinciding the lower boundary of the swirling high u_θ region. It appears that this snapshot corresponds to the phase at which the upstream end of the backflow vortex penetrates across the tip gap to the SS of the blade (Figs. 8(*g*), 8(*h*), and 9(*b*)). Figures 11(*a*) and 11(*b*) are other examples of the tip flow being disrupted by the BFV; this time at $s/c = 0.16$. A strong backflow with high u_θ rushes through the tip gap to the SS, disrupting the TLV and generating a radially inward spiraling "jet" that impinges on the blade surface. Such a flow structure differs significantly from the normal conditions depicted in Fig. 5(*a*). This violent flow disruption appears to cause formation of a new BFV at $r/L \sim 0.8$, well under the TLV, in the region of high u_θ gradients.

Before concluding this section, it should be noted that intermittent formation of backflow vortices is not limited to the present setup that has a relative wide tip gap. A series of such structures appear to form also under the high u_θ region of the same machine when the tip gap is narrow ($h/c = 0.5\%$), as demonstrated (e.g.,) in Figs. 11(*h*) and 11(*g*) in Ref. [28]. However, the narrow tip gap seems to inhibit the penetration of structures across the tip gap, greatly reducing "cross-talk" between passages.

Finally, considering that the upstream end of the backflow vortex makes it to the leading edge of the next blade, it would be of interest to conclude this part of the discussion by examining its impact on the flow there. The distribution of ensemble-averaged velocity for $\theta = 0$ and a sample snapshot of the flow when the backflow vortex reaches the leading edge are presented in Fig. 12. In the mean distribution, the leakage flow is minimal, and the magnitude of $<u_\theta>$ along the pressure side is significant, but mild. Conversely, in the selected instantaneous sample, u_θ over the entire PS is well above 80% of the tip speed, and there is a strong leakage flow, which brings fluid with elevated u_θ to the SS as well. Under the present prestall condition, such events are still quite intermittent, namely they occur in 40 out of the 2500 realizations, using high $<u_\theta>$ rushing through the gap as a criterion. The highly intermittency of this event is one of the indications that the presently described flow phenomena correspond to spike-type stall. Figure 13 demonstrates the impact of the backflow vortex and the high u_θ zone on the incidence angle $s/c = -0.16$, just upstream of the rotor blade leading edge. Figure 13(*a*) shows the location of $s/c = -0.16$ relative to the blade and defines the angle relative to the meridional plane depicted in the other plots, where the intersection of the blade tip leading edge with the r–z plane is illustrated by dashed line. Figure 13(*b*) presents the distribution of ensemble-averaged angle based on the entire database. In contrast, Fig. 13(*c*) shows the conditionally averaged angle using the criterion $u_\theta > 0.29U_T$ at the point indicated by a circle, which would be located in the tip gap once the blade arrives. This condition corresponds to the 100 most extreme cases (out of 2500) of backflow vortices reaching the leading edge of the next blade. As is evident, the BFV and associated high u_θ region cause a significant increase to the tip region incidence angle. As plotted in Fig. 13(*d*), the increase in incidence angle around the leading edge of the blade tip and to the right of it falls in the 4–10 deg range. Hence, for heavily loaded blades, such a change in incidence might cause leading edge separation, which has been proposed before as a mechanism affecting the onset of stall [17,18]. In addition to the changes in incidence angle, the increase in u_θ, namely a decrease in velocity relative to the blade, also affects the blade loading in the tip region. Consequently, as demonstrated in Fig. 9, the BFV-induced flow disrupts and delays the TLV rollup process. Figure 13(*d*) also show that the change to incidence angle (and decrease in relative velocity) is, for the most part, restricted to the tip region of the blade ($r/L > 0.8$).

Visualization of Flow Structures at Stall Conditions. As discussed before, readily noticed stall inception occurs and the pressure rise across the pump drops dramatically when the flow rate

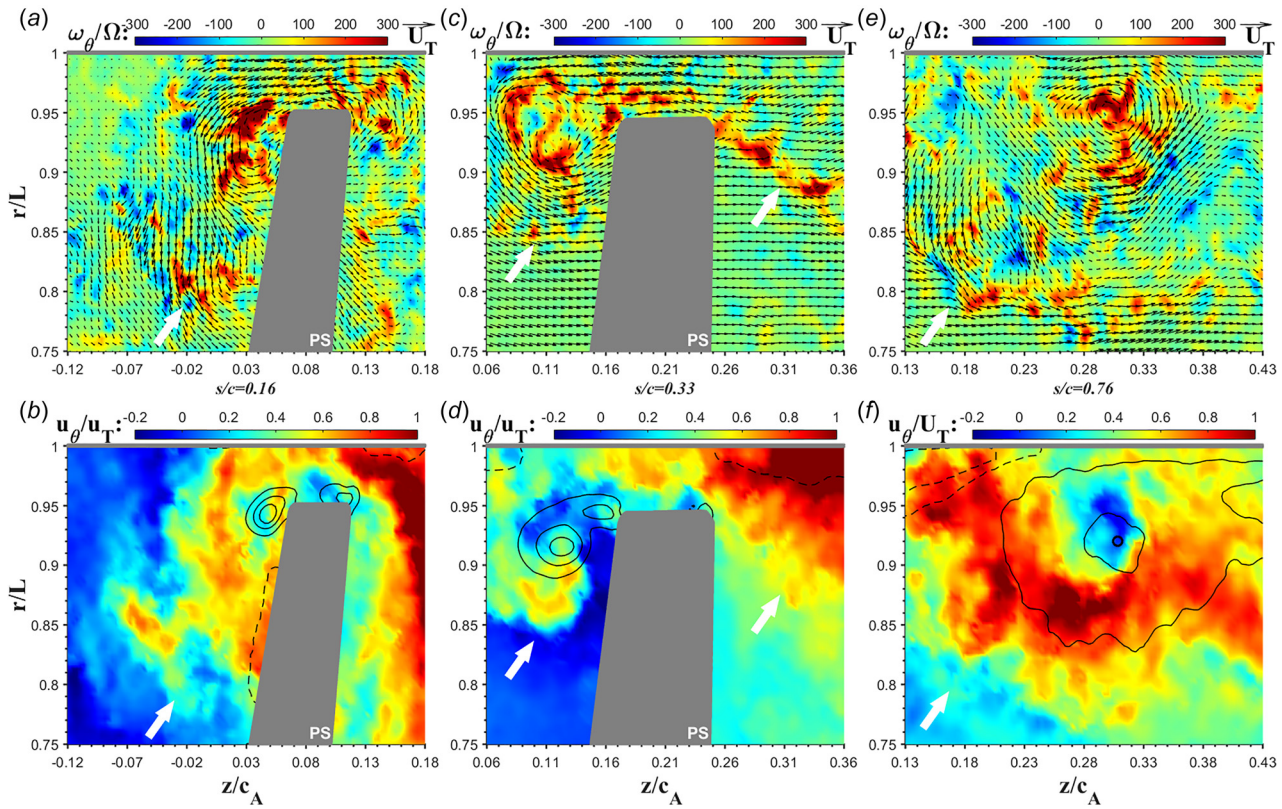

Fig. 11 Samples of instantaneous realizations of $<\omega_\theta>$ (top row) and $<u_\theta>$ (bottom row) at (*a*) and (*b*) $s/c = 0.16$, (*c*) and (*d*) $s/c = 0.33$ and (*e*) and (*f*) $s/c = 0.76$, when the backflow vortices interact with the adjacent blade. Vectors are diluted by 2:1 axially and 2:1 radially. Lines in (*b*), (*d*), and (*f*) are contours of $<\omega_\theta>$, with dashed lines indicating negative values.

Downloaded from http://asmedigitalcollection.asme.org/turbomachinery/article-pdf/139/4/041008/6305544/turbo_139_04_041008.pdf by Johns Hopkins University user on 08 December 2020

coefficient is reduced from $\varphi = 0.25$ to 0.24 (Fig. 2). The cavitation visualizations, samples of which are presented in Fig. 14, reveal that under this condition, the backflow vortices roll up earlier and appear more frequently, as well as grow more rapidly and to a considerable larger size compared to those at prestall condition. Hence, multiple backflow vortices frequently extend from the SS of the same blade at the same time. Yet, their appearance and process of development appear to have many of the same characteristic features. Their downstream ends appear to be connected to the SS of one blade, and the upstream ends extend well upstream of the leading edge of the adjacent blade or penetrating across the tip gap to the next passage, depending on their location. Propagation from upstream around the leading edge, which occurs frequently under stall conditions would presumably have more influence on the flow in the next passage than disturbances penetrating across the tip gap. In Fig. 14(*a*), the size of the newly formed backflow vortex indicated by an arrow is already comparable to that of a "fully developed" structure in Fig. 8(*d*). In Fig. 14(*b*), the vortex indicated by another arrow rolls up near the blade leading edge. These structures migrate mostly circumferentially with the blade, and slowly downstream, indicating that once they form, there is little through flow in the tip region.

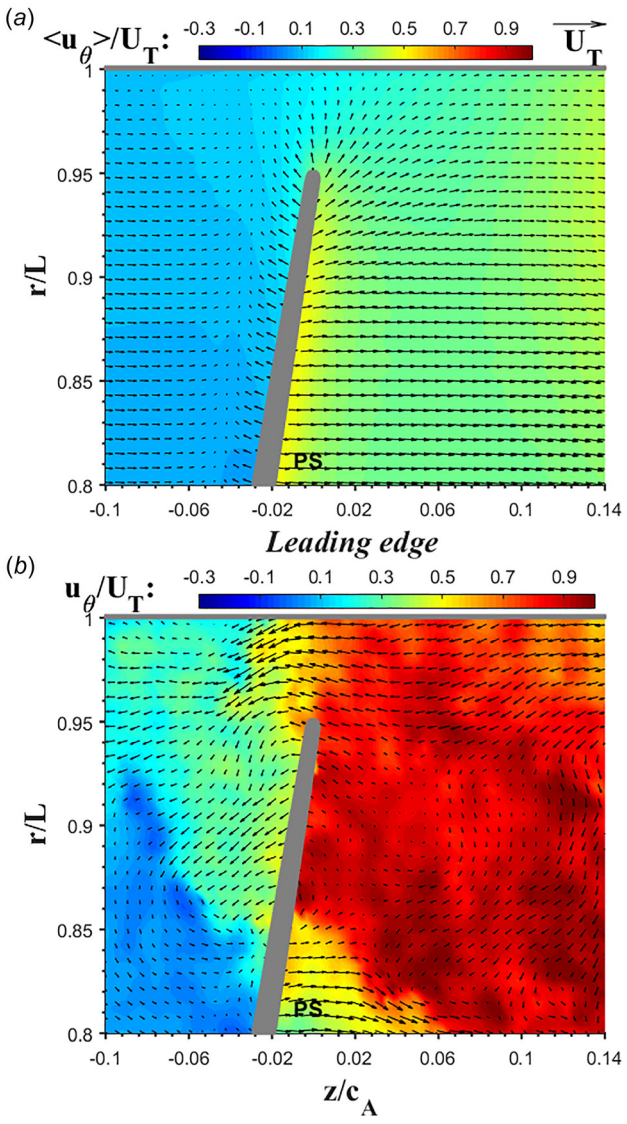

Fig. 12 (*a*) $<u_\theta>$ and (*b*) an instantaneous sample u_θ at the leading edge at $\varphi = 0.25$. Vectors are diluted by 2:1 axially and 2:1 radially.

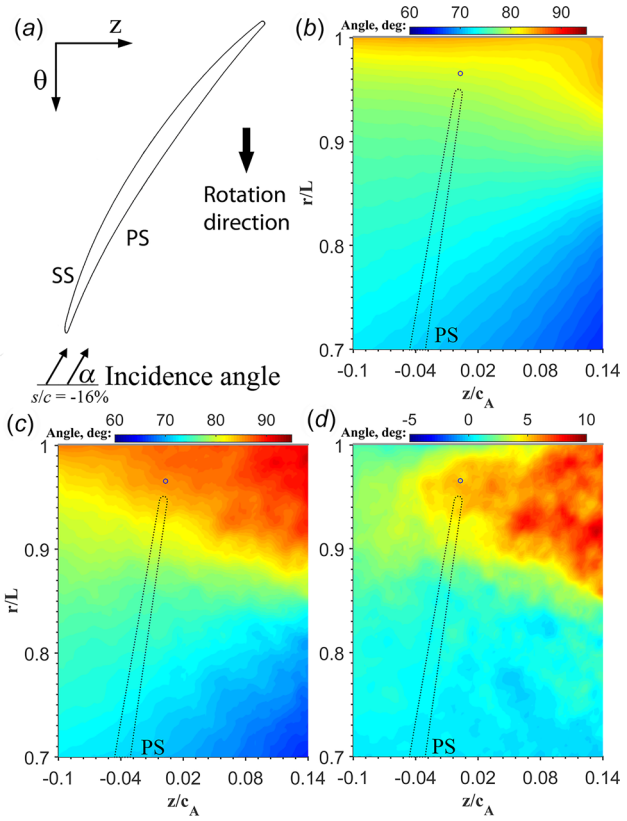

Fig. 13 Relative incidence angles (angles relative to the meridional plane) at $s/c = -0.16$. (*a*) A sketch showing the definition of incidence angle. (*b*) Ensemble-averaged result of 2500 realizations. (*c*) Conditionally averaged result of 100 extreme cases when backflow vortices reaching near the LE. (*d*) The change in incidence angle. Dot line indicates the location of the leading edge. The circle indicates the location used for conditional sampling.

Accordingly, when a backflow vortex begins to interact with the leading edge of the next blade, the TLV of that blade disappears completely, suggesting a loss of the lift force at least in the tip region. Such interactions might also induce leading edge separation, the process affecting stall onset according to Refs. [17] and [18]. It should be noted that this structure appears to be similar to that observed in Ref. [16] under deep stall, but in their case, the vortex appears to be fixed relative to the blade.

Discussion

Among the questions that the present measurements raise, it would be of interest to determine whether the phenomena described in this paper correspond to spike or modal type stall [7–12]. We have not performed wall pressure fluctuation measurements at the endwall casing at the onset of stall, so our assessment is suggestive, but not decisive. Several features of the available data at $\varphi = 0.25$ appear to be consistent with a spike-type stall described in Refs. [4] and [10]. First, the prestall condition, $\varphi = 0.25$, is still located at a slightly higher flow rate than the peak in the total-to-static performance curve. Second, the influence of the BFV on the flow around the leading edge of the next blade is intermittent, and quite infrequent under the prestall conditions. Third, once the flow around the leading edge is disrupted by the BFV, the effect, as Fig. 11 shows, is substantial covering the entire tip region of the blade. In other words, this is not a small perturbation. Fourth, yet, all the presently observed phenomena are confined to the tip region, where they are expected to generate high pressure fluctuations in the endwall casing. Conversely, at $\varphi = 0.24$, the slope of the *T*–*S* curve (Fig. 2(*b*)) is already positive,

Downloaded from http://asmedigitalcollection.asme.org/turbomachinery/article-pdf/139/4/041008/6305544/turbo_139_04_041008.pdf by Johns Hopkins University user on 08 December 2020

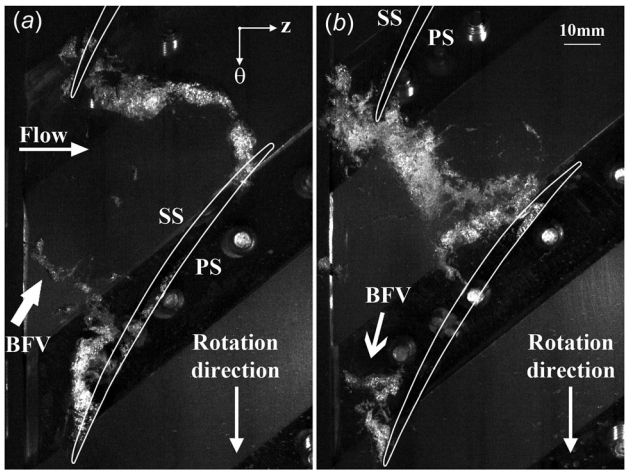

Fig. 14 Sample unrelated snapshots of huge backflow vortices in the rotor passage at stall conditions

consistent with trends of modal stall inception. The frequency of events is also much higher. However, as the present observations indicate, the flow phenomena triggering the performance loss at $\varphi = 0.24$ and 0.25 appear to be similar, but with increasing frequency and strength.

Another question is the relationship between the BFV and the tornado-like vortex described in Refs. [14], [15], and [17] and affiliated with the onset of stall. Both cases involve complete or partial ringlike vortical structure that surrounds the TLV. However, the formation mechanisms and locations involved are very different, since the BFV is not associated directly with leading edge separation, although it might cause one. In fact, in most of the present cases, the BFV is initiated downstream of the leading edge as a previous BFV propagates across the tip gap and causes rollup of the shear layer at the bottom of the high u_θ region. Furthermore, as discussed in Ref. [18], the tornado-like vortex does not necessarily require a backflow, whereas the present structures are an inherent outcome of backward leakage flow.

Before concluding, it should be noted that backflow vortices are also observed at much higher flow rates than the current prestall and stall conditions. However, at $\varphi = 0.35$, for example, rollup of these structures occurs in the aft part of the rotor passage, they are much more intermittent, and for the most part they appear to be much weaker. Hence, they are mostly entrained by the TLV before it bursts, and rarely make it to the tip gap of the next blade. Also, as noted before, in a parallel study focusing on the effects of the tip gap size on the flow structures of the same machine [36] and in Ref. [28], similar backflow vortices have been observed when the tip gap is much narrower ($h/c = 0.5\%$). However, since the BFV cannot be entrained across the narrow tip gap, its influence on the adjacent blade passage is greatly diminished. Furthermore, occurrence and persistent formation of BFVs is not limited to the present blade geometries. For example, the BFV and vortical layers emerging from the tip gap have been seen in previous measurements performed within a waterjet pump [26,29]. Although the presently available data are limited to three pump/compressor geometries, several flow rates, and two tip gaps for the present compressor, the backflow vortices, and mechanisms generating them appear with varying degrees of influence in all of them. The formation of a backflow vortex and its association with tip leakage flows appear to be a ubiquitous phenomenon.

Finally, another question involves the influence of the IGV and its wakes on the formation and development of the BFV. We have not studied this effect based on velocity measurements yet. However, systematic evaluations of the cavitation movies clearly show that appearance and development of the BFV do not occur at specific circumferential angles relative to the IGV blades. In a field of view that covers three IGV blades, the vortex appears intermittently at different locations. Moreover, similar backflow vortices appear in the abovementioned axial waterjet pumps that do not have IGVs. However, these observations do not necessarily imply that the nonuniform inflow does not affect the strength, trajectory, and influence of the BFVs. We will explore this question in future studies.

Conclusions

Stereoscopic PIV measurements and cavitation-based flow visualizations are used for resolving flow structures characterizing prestall and early stall conditions in the tip region of the rotor passage of an axial compressor. The experiments have been performed in the JHU optically index-matched facility, which facilitates unobstructed observations on the origin and evolution of flow features at any desired point. All the flow instabilities affecting the onset of stall are associated with the 3D tip leakage flow and its interaction with the rest of the passage flow. As the tip leakage vortex rolls up, it entrains the leakage flow and forms a region with high circumferential velocity (low circumferential velocity relative to the blade) under the vortex center. Hence, the flow in the tip region could be envisioned as a 3D swirling jet in which the center of swirl is located above the jet center. In the ensemble-averaged 3D vorticity distributions, obtained by combining data recorded in a series of closely spaced meridional planes, this jet appears as a vortex ring that surrounds the tip leakage vortex. As the TLV grows in size, detaches from the blade SS, and breaks down in the middle of the passage, the size of the elevated circumferential velocity region expends, eventually reaching the pressure side of the adjacent blade. The vorticity at the transition between the high circumferential velocity region below the TLV center and the main flow deeper in the passage is oriented nearly perpendicularly to the blade surface. Once this vortical region is perturbed, it rolls up into a vortex segment that extends diagonally upstream, from the vicinity of the suction side (SS) of the originating blade, to the edge of the elevated circumferential velocity region (where the vorticity changes direction). Due to its orientation, we refer to this structure as a backflow vortex (BFV), adopting the terminology used to describe vortices extending upstream of rocket fuel inducers [31–33].

As the SS end of the BFV propagates in the passage, it grows in length and intermittently reaches the pressure side of the next blade together with the high u_θ zone above it. For the present large tip gap, the BFV and high u_θ zone readily propagate across the tip gap to the SS of the adjacent blade and trigger a similar instability in the next passage. Hence, once it starts, the process propagates circumferentially from one passage to the next. As it crosses the tip gap, the BFV and high u_θ zone alter the blade load distributions, as demonstrated by the major shift in the location of TLV rollup on this blade. Although the ensemble-averaged 3D vorticity distributions cannot reveal the structure of such intermittent phenomena, a small fraction ($\sim$4%) of the instantaneous planar snapshots bear clear signatures of the BFV, which includes a series of vortical structures bounding the bottom side of a very high u_θ zone, where the passage flow is essentially blocked. These snapshots reveal a flow structure that differs substantially from the normal SS flow condition when the passage is not stalled.

BFVs of varying strengths and locations have been seen in rotors having a narrow tip clearance, but in these cases, they cannot propagate to the next passage across the tip gap. The same flow phenomenon also causes intermittent but significant changes to the incidence angle upstream of the blade leading edge. Such incidence changes might cause leading edge flow separation in some machines, as observed at the onset of stall in other studies, but it does not appear to occur for the present prestall flow. Although we have not measured the pressure fluctuations in the endwall casing, several features of the BFV development process described in this paper at prestall conditions are consistent with spike-type stall [7–10]. Included are the location of the prestall condition in the performance curve, intermittent appearance and

Downloaded from http://asmedigitalcollection.asme.org/turbomachinery/article-pdf/139/4/041008/6305544/turbo_139_04_041008.pdf by Johns Hopkins University user on 08 December 2020

effect on the flow around the leading edge of the blade, and confinement to the tip region.

By further reducing the flow rate and pushing the present machine into stall conditions, the size and frequency of the BFVs increase substantially, and they extend upstream of the leading edge of the adjacent blade. Hence, they can propagate to the next passage and trigger instabilities there without being ingested across the tip gap. Furthermore, they alter the blade loading, as indicated by the delayed TLV rollup.

Acknowledgment

This project has been funded by NASA. The authors would like to thank Chunill Hah and Michael Hathaway from NASA/Glenn for their guidance, and for modifying the LSAC blade geometries to match the constraints of the JHU index-matched facility. We would also like to express our gratitude to Yury Ronzhes who designed all the mechanical components of this facility.

Nomenclature

c = rotor blade tip chord
h = width of the rotor blade tip gap
H = rotor blade span
k^* = turbulent kinetic energy
L = nominal distance from the hub to the inner casing endwall
p_{exit} = static pressure at stator outlet
p_{in} = static pressure at IGV inlet
p_{0i} = total pressure at IGV inlet
r, z, θ = radial, axial and circumferential coordinates
s = rotor blade chordwise coordinate
t^* = normalized time
u_r, u_z, u_θ = radial, axial and circumferential velocity
U_T = rotor blade tip speed
u' = velocity fluctuation
ρ = NaI solution density
φ = flow coefficient
ψ_{SS} = static-to-static pressure rise coefficient
ψ_{TS} = total-to-static pressure rise coefficient
$\omega_r, \omega_z, \omega_\theta$ = radial, axial and circumferential vorticity
Ω = rotor angular velocity
$< >$ = ensemble-averaged quantity

References

[1] Pampreen, R. C., 1993, *Compressor Surge and Stall*, Concepts ETI, Norwich, VT.
[2] Fukano, T., and Jang, C. M., 2004, "Tip Clearance Noise of Axial Flow Fans Operating at Design and Off-Design Condition," J. Sound Vib., **275**(3), pp. 1027–1050.
[3] Schoenenborn, H., and Breuer, T., 2012, "Aeroelasticity at Reversed Flow Conditions—Part II: Application to Compressor Surge," ASME J. Turbomach., **134**(6), p. 061031.
[4] Day, I. J., 2016, "Stall, Surge and 75 Years of Research," ASME J. Turbomach., **138**(1), p. 011001.
[5] Emmons, H. W., Person, C. E., and Grant, H. P., 1955, "Compressor Surge and Stall Propagation," Trans. ASME, **77**(4), pp. 455–469.
[6] Greitzer, E. M., 1976, "Surge and Rotating Stall in Axial Flow Compressors—Part I: Theoretical Compression System Model," ASME J. Eng. Power, **98**(2), pp. 190–198.
[7] Day, I. J., 1993, "Stall Inception in Axial Flow Compressors," ASME J. Turbomach., **115**(1), pp. 1–9.
[8] McDougall, N. M., Cumpsty, N. A., and Hynes, T. P., 1990, "Stall Inception in Axial Compressors," ASME J. Turbomach., **112**(1), pp. 116–123.
[9] Garnier, V. H., Epstein, A. H., and Greitzer, E. M., 1991, "Rotating Waves as a Stall Inception Indication in Axial Compressors," ASME J. Turbomach., **113**(2), pp. 290–301.
[10] Camp, T. R., and Day, I. J., 1998, "A Study of Spike and Modal Stall Phenomena in a Low-Speed Axial Compressor," ASME J. Turbomach., **120**(7), pp. 393–401.
[11] Deppe, A., Saathoff, H., and Stark, U., 2005, "Spike-Type Stall Inception in Axial-Flow Compressors," 6th European Conference on Turbomachinery, Lille, France, Mar. 7–11, pp. 178–188.
[12] Tan, C. S., Day, I., Morris, S., and Wadia, A., 2010, "Spike-Type Compressor Stall Inception, Detection, and Control," Annu. Rev. Fluid Mech., **42**(1), pp. 275–300.
[13] Vo, H. D., Tan, C. S., and Greitzer, E. M., 2008, "Criteria for Spike Initiated Rotating Stall," ASME J. Turbomach., **130**(1), p. 011023.
[14] Inoue, M., Kuroumaru, M., Tanino, T., Yoshida, S., and Furukawa, M., 2001, "Comparative Studies on Short and Long Length-Scale Stall Cell Propagating in an Axial Compressor Rotor," ASME J. Turbomach., **123**(1), pp. 24–32.
[15] Inoue, M., Kuroumaru, M., Yoshida, S., and Furukawa, M., 2002, "Short and Long Length-Scale Disturbances Leading to Rotating Stall in an Axial Compressor Stage With Different Stator/Rotor Gaps," ASME J. Turbomach., **124**(3), pp. 376–384.
[16] Kosyna, G., Goltz, I., and Stark, U., 2005, "Flow Structure of an Axial-Flow Pump From Stable Operation to Deep Stall," ASME Paper No. FEDSM2005-77350.
[17] Yamada, K., Kikuta, H., Iwakiri, K., Furukawa, M., and Gunjishima, S., 2013, "An Explanation for Flow Features of Spike-Type Stall Inception in an Axial Compressor Rotor," ASME J. Turbomach., **135**(2), p. 021023.
[18] Pullan, G., Young, A. M., Day, I. J., Greitzer, E. M., and Spakovszky, Z. S., 2015, "Origins and Structure of Spike-Type Rotating Stall," ASME J. Turbomach., **137**(5), p. 051007.
[19] Everitt, J. N., and Spakovszky, Z. S., 2012, "An Investigation of Stall Inception in Centrifugal Compressor Vaned Diffuser," ASME J. Turbomach., **135**(1), p. 011025.
[20] Hoying, D. A., Tan, C. S., Vo, H. D., and Greitzer, E. M., 1999, "Role of Blade Passage Flow Structurs in Axial Compressor Rotating Stall Inception," ASME J. Turbomach., **121**(4), pp. 735–742.
[21] Hah, C., Bergner, J., and Schiffer, H.-P., 2006, "Short Length-Scale Rotating Stall Inception in a Transonic Axial Compressor—Criteria and Mechanisms," ASME Paper No. GT2006-90045.
[22] Mathioudakis, K., and Breugelmans, F. A. E., 1985, "Development of Small Rotating Stall in a Single Stage Axial Compressor," ASME Paper No. 85-GT-227.
[23] Mailach, R., Lehmann, I., and Vogeler, K., 2001, "Rotating Instabilities in an Axial Compressor Originating From the Fluctuating Blade Tip Vortex," ASME J. Turbomach., **123**(3), pp. 453–463.
[24] März, J., Hah, C., and Neise, W., 2002, "An Experimental and Numerical Investigation Into the Mechanisms of Rotating Instability," ASME J. Turbomach., **124**(3), pp. 367–375.
[25] Young, A., Day, I., and Pullan, G., 2012, "Stall Warning by Blade Pressure Signature Analysis," ASME J. Turbomach., **135**(1), p. 011033.
[26] Wu, H., Tan, D., Miorini, R. L., and Katz, J., 2011, "Three-Dimensional Flow Structures and Associated Turbulence in the Tip Region of a Waterjet Pump Rotor Blade," Exp. Fluids, **51**(6), pp. 1721–1737.
[27] Miorini, R. L., Wu, H., and Katz, J., 2012, "The Internal Structure of the Tip Leakage Vortex Within the Rotor of an Axial Waterjet Pump," ASME J. Turbomach., **134**(3), p. 031018.
[28] Tan, D., Li, Y., Wilkes, I., Miorini, R., and Katz, J., 2015, "Visualization and Time Resolved PIV Measurements of the Flow in the Tip Region of a Subsonic Compressor Rotor," ASME J. Turbomach., **137**(4), p. 041007.
[29] Wu, H., Miorini, R. L., and Katz, J., 2011, "Measurements of the Tip Leakage Vortex Structures and Turbulence in the Meridional Plane of an Axial Water-Jet Pump," Exp. Fluids, **50**(4), pp. 989–1003.
[30] Wu, H., Miorini, R. L., Tan, D., and Katz, J., 2012, "Turbulence Within the Tip-Leakage Vortex of an Axial Waterjet Pump," AIAA J., **50**(11), pp. 2574–2587.
[31] Yamanishi, N., Fukao, S., Qiao, X., Kato, C., and Tsujimoto, Y., 2007, "LES Simulation of Backflow Vortex Structure at the Inlet of an Inducer," ASME J. Fluids Eng., **129**(5), pp. 587–594.
[32] Yamamoto, K., and Tsujimoto, Y., 2009, "Backflow Vortex Cavitation and Its Effects on Cavitation Instabilities," Int. J. Fluid Mach. Syst., **2**(1), pp. 40–54.
[33] Yokota, K., Kurahara, K., Kataoka, D., Tsujimoto, Y., and Acosta, A. J., 1999, "A Study of Swirling Backflow and Vortex Structure at the Inlet of an Inducer," JSME Int. J., Ser. B, **42**(3), pp. 451–459.
[34] Hah, C., Hathaway, M., and Katz, J., 2014, "Investigation of Unsteady Flow Field in a Low-Speed One and a Half Stage Axial Compressor, Part 2: Effects of Tip Gap Size on the Tip Clearance Flow Structure at Near Stall Operation," ASME Paper No. GT2014-27094.
[35] Bai, K., and Katz, J., 2014, "On the Refractive Index of Sodium Iodide Solutions for Index Matching in PIV," Exp. Fluids, **55**(4), pp. 1–6.
[36] Li, Y., Chen, H., Tan, D., and Katz, J., 2016, "Effects of Tip Clearance and Operating Conditions on the Flow Structure and Reynolds Stresses Within an Axial Compressor Rotor Passage," ASME Paper No. GT2016-57050.
[37] Wieneke, B., 2005, "Stereo-PIV Using Self-Calibration on Particle Images," Exp. Fluids, **39**(2), pp. 267–280.
[38] Adrian, R., and Westerweel, J., 2011, *Particle Image Velocimetry*, Cambridge University Press, New York, pp. 241–248.
[39] Roth, G. I., and Katz, J., 2001, "Five Techniques for Increasing the Speed and Accuracy of PIV Interrogation," Meas. Sci. Technol., **12**(3), pp. 238–245.
[40] Westerweel, J., and Scarano, F., 2005, "Universal Outlier Detection for PIV Data," Exp. Fluids, **39**(6), pp. 1096–1100.
[41] Schrapp, H., Stark, U., Goltz, I., Kosyna, G., and Bross, S., 2004, "Structure of the Rotor Tip Flow in a Highly-Loaded Single-Stage Axial-Flow Pump Approaching Stall. Part I: Breakdown of the Tip-Clearance Vortex," ASME Paper No. HT-FED2004-56780.
[42] Yamada, K., Furukawa, M., Nakano, T., and Inoue, M., 2004, "Unsteady Three-Dimensional Flow Phenomena Due to Breakdown of Tip Leakage Vortex in a Transonic Axial Compressor Rotor," ASME Paper No. GT2004-53745.

Downloaded from http://asmedigitalcollection.asme.org/turbomachinery/article-pdf/139/4/041008/6305544/turbo_139_04_041008.pdf by Johns Hopkins University user on 08 December 2020

[43] Furukawa, M., Inoue, M., Saiki, K., and Yamada, K., 1998, "The Role of Tip Leakage Vortex Breakdown in Compressor Rotor Aerodynamics," ASME Paper No. 98-GT-239.
[44] Tan, D., Li, Y., Chen, H., Wilkes, I., and Katz, J., 2015, "The Three Dimensional Flow Structure and Turbulence in the Tip Region of an Axial Flow Compressor," ASME Paper No. GT2015-43385.
[45] Yu, X., Liu, B., and Jiang, H., 2007, "Characteristics of the Tip Leakage Vortex in a Low-Speed Axial Compressor," AIAA J., **45**(4), pp. 870–878.
[46] Yokota, K., Mitsuda, K., Tsujimoto, Y., and Kato, C., 2004, "A Study of Vortex Structure in the Shear Layer Between Main Flow and Swirling Backflow," JSME Int. J., Ser. B, **47**(3), pp. 541–548.

Downloaded from http://asmedigitalcollection.asme.org/turbomachinery/article-pdf/139/4/041008/6305544/turbo_139_04_041008.pdf by Johns Hopkins University user on 08 December 2020